ACS OMEGA

Open Access

http://pubs.acs.org/journal/acsodf

Article

Effect of Crystal Morphology on Electrochemical Performances of IRH-2 and IRH-2/PANI Composite for Supercapacitor Electrodes

Najmeddine Ferhi,* Mohamed Essalhi, and Ramzi Zarrougui*

Cite This: *ACS Omega* 2023, 8, 43708−43718

Read Online

ACCESS | Metrics & More | Article Recommendations | Supporting Information

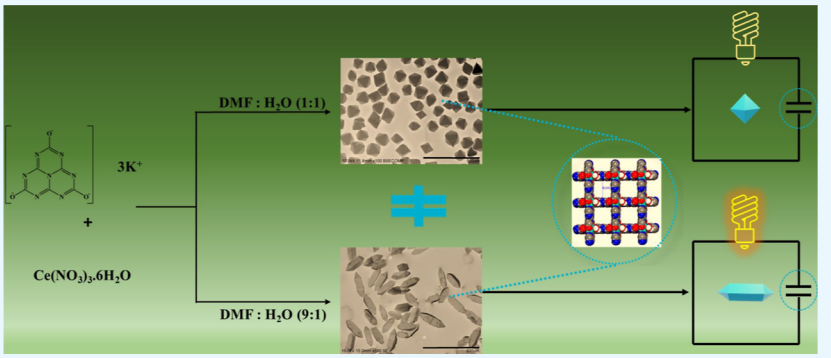

ABSTRACT: In the context of recent progress in designing metal−organic framework (MOF)-based supercapacitor electrodes, we report herein the successful growth of two different crystal morphologies of a cerium-based MOF, octahedral crystals named IRH-2-O and elongated square-bipyramidal crystals named IRH-2-ESBP (IRH = *Institute de Recherche sur l'Hydrogène*). The identical crystal structure of both materials was confirmed by powder X-ray diffraction (PXRD). Furthermore, scanning electron microscopy and energy-dispersive X-ray mapping analysis corroborated this fact and showed the crystal shape variation *versus* the surface composition of synthesized materials. Fourier transform infrared spectroscopy, UV−vis spectroscopy, and PXRD were used to confirm the purity of pristine MOFs as well as desired MOF//PANI composites. Cyclic voltammetry and electrochemical impedance spectroscopy highlighted the effect of crystal shape on the electrochemical performance of IRH-2 MOFs; the specific capacitance tripled from 43.1 $F{\cdot}g^{-1}$ for IRH-2-O to 125.57 $F{\cdot}g^{-1}$ for IRH-2-ESBP at 5 $mV{\cdot}s^{-1}$. The cycling stability was notably ameliorated from 7 K for IRH-2-O to 20 K for IRH-2-ESBP. Regarding the composites, the cell voltage was notably ameliorated from 1.8 to 1.95 V. However, the electrochemical performance of IRH-2/PANI composites was drastically decreased due to instability in the acidic media. To the best of our knowledge, our work is the first work that related the MOF crystal shape and the electrochemical performance.

INTRODUCTION

Energy-related challenges have been a significant issue for many years and continue to pose major obstacles due to various factors.[1−3] These include the rapid growth in energy demand,[4−6] pollution resulting from the excessive use of fossil fuels,[7,8] and the increasing reliance on energy-dependent technologies.[9] The way we address these energy difficulties will play a crucial role in shaping the future development of humanity.[10] Renewable energy resources offer interesting alternatives to fossil fuels for electricity generation;[11−14] however, the intermittent nature of these resources necessitates the development of adequate energy storage devices to handle production fluctuations.[15,16]

A wide range of electric energy storage (EES) devices have been developed, such as metal-ion batteries,[17,18] metal−air batteries,[19−22] capacitors, supercapacitors, and a hybrid device known as a supercapbattery or supercapattery.[23,24] Supercapacitors have garnered significant attention in various electronic industries due to their ability to store electricity electrostatically through ultrafast oxidoreductive reactions,[25−27] resulting in high capacitance.[28−30] They are renowned for their safety, reliable cyclability, and rapid charging and discharging rates.[31−33] Researchers are focusing on electrode materials that can combine the electric double layer (EDLC) mechanism and the pseudocapacitive mechanism to enhance these features. Such hybrid materials facilitate faster redox reactions, increase the energy density, and provide a larger accessible specific surface area for the EDLC mechanism to function.[34−36]

Received: July 24, 2023
Revised: October 19, 2023
Accepted: October 24, 2023
Published: November 8, 2023

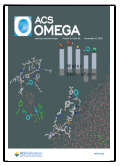

Among the promising electrode materials, 2D materials,[37−39] including graphene and its derivatives,[40,41] as well as porous materials, like metal−organic frameworks (MOFs),[42−46] have shown potential. MOFs stand out due to their high surface area, tunable porosity, and thermal and chemical stability. Their heterogeneous composition makes them advantageous for use as oxidoreductive materials while offering the necessary accessible surface area for the EDLC mechanism. Utilizing MOFs can address the limitations of supercapacitors by providing additional active surface area for electrochemical processes and ensuring redox reactions to increase the energy density.

Although extensive research has been conducted on MOFs as supercapacitor electrodes in the past decade,[47−49] limited attention has been given to cerium-based MOFs. Only a few studies on this topic have been reported in the literature.[49−51] Therefore, this study aims to explore the electrochemical performance of cerium-based IRH-2[52] and its composites as supercapacitor electrodes. Specifically, we investigate the impact of varying crystal morphologies[53−55] of cerium-based IRH-2, ranging from octahedral to elongated square-bipyramidal shapes. Additionally, we examine the influence of combining these morphologies with polyaniline (PANI) on their electrochemical properties. The primary objective of this work is to study the anisotropic/isotropic crystal growth of different forms of IRH-2 and their composites under various reaction conditions, highlighting how crystal shape and morphology affect their performance as supercapacitor electrodes.

EXPERIMENTAL SECTION

Instrumentation/Materials Characterizations. The attenuated total reflection (ATR) method was used for Fourier transform infrared (FTIR) characterization. Background spectra were collected before inserting the powder samples in the pellet holder for measurements. Spectra were collected with a Nicolet iS 10 Smart FTIR spectrometer within the 500−4000 cm^{-1} range. Thermogravimetric (TG) analyses were performed using a Diamond Pyris 6000 TGA/DTA apparatus from PerkinElmer, with temperatures ranging from 30 to 800 °C at a heating rate of 5 °C·min^{-1} under a N_2 flow of 20 mL·min^{-1}. Single-crystal X-ray diffraction (SCXRD) and powder X-ray diffraction (PXRD) data were collected at room temperature on the Incoatec Microfocus high-brilliance source Bruker diffractometer. Prior to measurements, all PXRD samples were gently ground, then a small amount of powder was mounted on a nylon loop. UV−vis spectra were recorded on a Cary 5000 spectrometer. The compounds were first dissolved in *N*-methyl-2-pyrrolidone (NMP) which was used as a blank for these measurements. Scanning electron microscopy (SEM) analysis was performed using a Hitachi SU1510 microscope.

Electrochemical Measurements. A carbon thin film was prepared by mixing active material with acetylene black and polytetrafluoroethylene binder in a ratio of 90:5:5 wt %. These three components were mixed in a small volume of ethanol (1 mL) until a homogenized suspension was obtained with a paste-like consistency. Final films were prepared from these suspensions by cold rolling. The resulting films were of 1 cm^2 in size and *ca.* 30 mg in weight. Then, they were placed on a stainless-steel grid (80 mesh, 0.127 mm thickness, Alfa Aesar) used as a current collector and pressed at 15 × 10^6 Pa for 1 h. Electrochemical measurements were performed in a one-compartment cell using a three-electrode configuration. An $Ag/AgCl/Cl^-$ (saturated KCl) electrode was used as a reference, while a high surface area platinum gauze served as the counter electrode. The working electrode was the MOF electrode film. A deaerated 3 M KOH solution was used as an electrolyte, and all experiments were performed at room temperature. The reference electrode was kept at about 5 mm of the working electrode during all measurements. Moreover, prior to any measurement, the working electrode was dipped in the electrolyte and degassed under a N_2 atmosphere for 30 min to allow the removal of O_2 and push the electrolyte to infuse through the porous structure of the electrode material. In all cases, three replicates were prepared and analyzed. Cyclic voltammetry (CV) measurements were recorded using an electrochemical workstation ZAHNER IM6 monitored by Thales software. The specific capacitance C_s, expressed in farads per gram ($F{\cdot}g^{-1}$) of the tested electrode, was determined from the CV curve according to eq 1

$$C_s = \frac{\Delta Q}{\Delta E \times m} \tag{1}$$

where ΔQ is the voltammetric charge (coulomb), ΔE is the cell voltage (volt), and m is the mass of the electrode active material (gram).

MATERIALS SYNTHESIS

Potassium Cyamelurate. Potassium cyamelurate ($K_3{\cdot}Cy$) was synthesized according to the method described in the literature reported by J. R. Holst *et al.*[56] A suspension of 25 g of melon in 250 mL of a 2.5 molar aqueous KOH solution was refluxed for 45 min. The hot reaction mixture was filtered and slowly cooled to 20 °C. The fine needles of potassium cyamelurate precipitated from the filtrate, were separated, washed off with ethanol, and dried at 100 °C under a vacuum.

IRH-2-O. Synthesis was carried out according to the solvothermal method as published by Mohan *et al.*[52] with some modifications using an equimolar mixture of *N*,*N*-dimethylformamide (DMF) and H_2O. Typically, 160 mg of potassium cyamelurate was solubilized in 50 mL of H_2O, and 1.3 g of cerium salt was solubilized in 50 mL of *N*,*N*-dimethylformamide (DMF). Then, solutions were mixed at room temperature, stirred, and sonicated for 15 min. Thereafter, the mixture was sealed and heated at 80 °C for 24 h. After cooling down to 60 °C, the as-synthesized IRH-O (octahedral colorless crystals) was recovered by filtration and washed twice with methanol (90% yield based on Cy).

IRH-2-ESBP. Synthesis was carried out according to the solvothermal method using a mixture of *N*,*N*-dimethylformamide (DMF) and H_2O (9:1). Typically, 160 mg of potassium cyamelurate was solubilized in 12 mL of H_2O, and 1.3 mg of cerium salt was solubilized in 108 mL of *N*,*N*-dimethylformamide (DMF). Then, solutions were mixed at room temperature, stirred, and sonicated for 15 min. Thereafter, the mixture was sealed and heated at 80 °C for 24 h. After cooling down to 60 °C, the as-synthesized IRH-2-O (octahedral colorless crystals) was recovered by filtration and washed twice with methanol (90% yield based on Cy). **PANI**. Nanofibers of PANI were synthesized by a modified method from literature.[57,58] Solution (A) was prepared by dissolving 0.93 g of aniline in 30 mL of HCl solution (1.0 M). The aniline solution was then mixed with 1 mL of absolute alcohol. 2.28 g of ammonium persulfate (APS) was dissolved in another 20 mL of HCl solution (1 M) to form solution (B). Solutions (A)

https://doi.org/10.1021/acsomega.3c05385
ACS Omega 2023, 8, 43708−43718

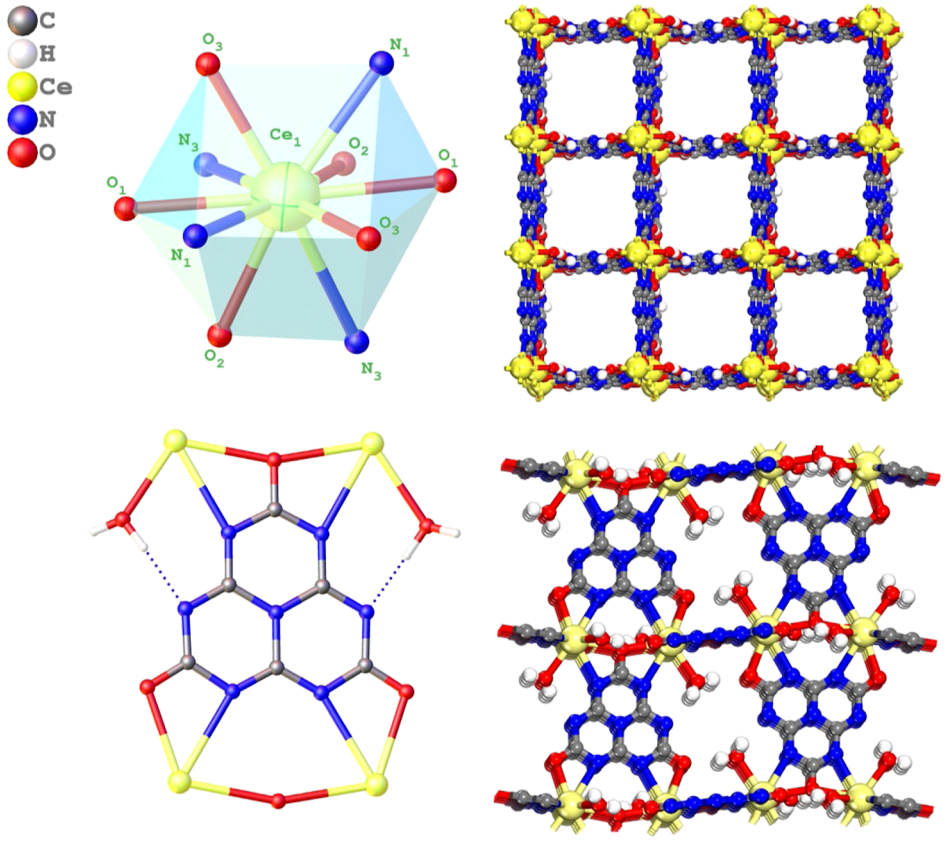

Figure 1. Coordination mode of the Cy linker and Ce metal nodes in the IRH-2 structure (right). Crystal structure of the extended 3D framework of IRH-2 (left).

and (B) were precooled for 20 min at 0−4 °C and then solution (B) was added into the above solution (A), mixed quickly, and stirred at room temperature. The polymerization proceeded for 30 min, and then the resulting deep green product was washed with excess ethanol and water and dried at 60 °C overnight.

IRH-2/PANI Composites. IRH-2 was degassed overnight at 120 °C under reduced pressure. Then, aniline monomers were absorbed in the activated IRH-2 channels at room temperature for 15 min upon applying reduced pressure and ultrasound.[59] 0.6 g of activated IRH-2 was mixed with 10 μL of aniline and mixed well with a mixing paddle followed by continuous ultrasonic shock and reduced pressure for 20 min. Then, 0.5 mL of 1 M HCl solution was added with ultrasonic shock for 10 min (removing the decompression device) to form solution (A). 2.28 g APS was dissolved in 20 mL of HCl solution (1 M) to form solution (B). Solutions (A) and (B) were precooled for 20 min at 0−4 °C and then solution (B) was added into the above solution (A), mixing quickly and stirring at room temperature. The polymerization proceeded for 30 min, and then the resulting deep green product (IRH-2/PANI) was washed with excess ethanol and water and dried at 60 °C overnight (Figure 1).

RESULTS AND DISCUSSION

SCXRD, PXRD, SEM/EDX (energy-dispersive X-ray), and FTIR have been performed to confirm the anisotropic/isotropic growth of IRH-2, depicting the identical crystal structure of the obtained octahedral (IRH-2-O) and elongated square-bipyramid crystals (IRH-2-ESBP). Figure 2 shows almost the same PXRD pattern for IRH-2-O and IRH-2-ESBP. Also, the conducted SCXRD analysis shows the same structure as the IRH series published by Mohan *et al.* and affirms the identical crystal structure for both synthesized phases (see Supporting Information). Additionally, IRH-2/PANI composites show well-matched PXRD patterns which highlight the same structural behavior of IRH-2-O and IRH-2-ESBP with PANI and further confirm their identical starting structure.

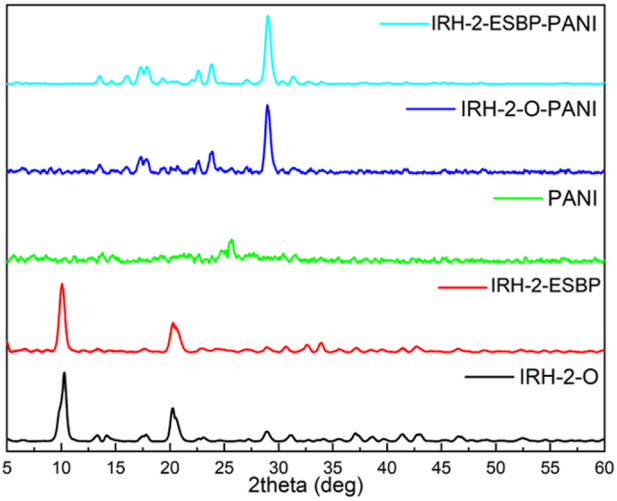

Figure 2. PXRD of synthesized materials.

SEM/EDX Mapping. The structural regulation of MOFs and their use in composite materials in terms of distribution and homogeneity largely depend on their crystal morphology

https://doi.org/10.1021/acsomega.3c05385
ACS Omega 2023, 8, 43708−43718

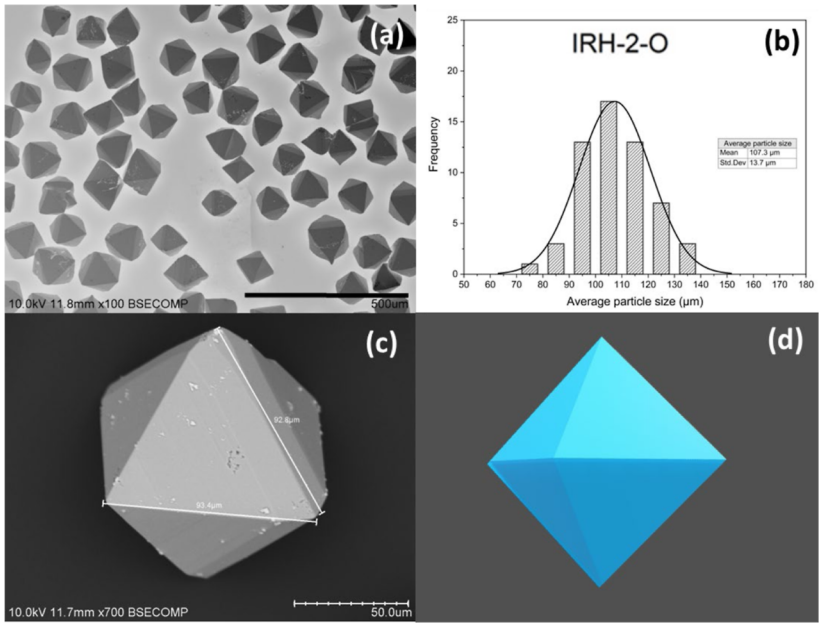

Figure 3. (a,c) SEM micrographs, (b) crystal size distribution, and (d) illustration of the octahedral shape of IRH-2-O.

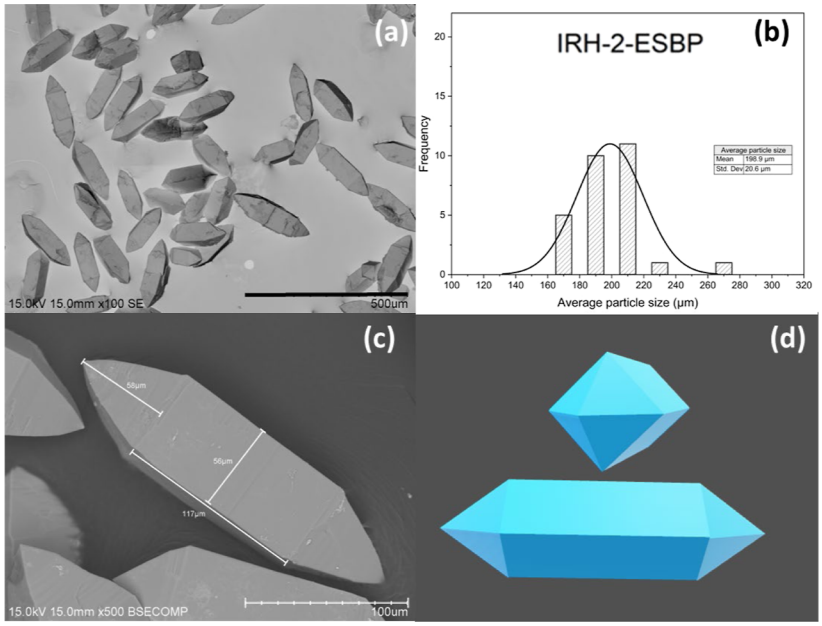

Figure 4. (a,c) SEM micrographs, (b) crystal size distribution, and (d) illustration of the octahedral shape of IRH-2-ESBP.

and their anisotropic crystal growth during synthesis.[59] Most microporous MOFs exhibit anisotropic and nonspherical shapes, illustrating their highly crystalline nature.[59] Anisotropic MOFs also exhibit different properties following different special axes and regions, such as metal nodes and ligand density in the exposed surface of crystals, surface charge and energy, curvature, and permeability and diffusivity of solvents and electrolytes.[60,61] Optimization of this parameter can significantly improve the electrochemical efficiency of electrode materials used for supercapacitors. In the case of IRH-2 materials, intrinsic parameters, such as the surface density of the cerium nodes and the nitrogen active sites of the Cy linkers, as well as the diffusivity of the electrolyte in the electrode material, were enhanced according to the tunable anisotropic and isotropic crystal growth of IRH-2, which leads to the improvement of electrochemical features of these materials and its polyaniline-based composite.

Two different crystal forms were obtained for IRH-2 named IRH-2-O and IRH-2-ESBP under two different solvothermal conditions. The equimolar mixture of DMF/H_2O leads to an isotropic growth of a homogeneous phase of octahedral crystals with an average particle size of 107.3 ± 13.7 μm (Figure 3a−d). In parallel, increasing the DMF amount in the reaction mixture to 90% leads to anisotropic growth of the elongated square-bipyramidal crystals of IRH-2-ESBP with an average particle size of 198.9 ± 20.6 μm, as shown in Figure 4. This variation can be explained by the preferential nucleation of the crystals along the *c*-axis due to the abundant presence of DMF molecules in the reaction medium.

https://doi.org/10.1021/acsomega.3c05385
ACS Omega 2023, 8, 43708−43718

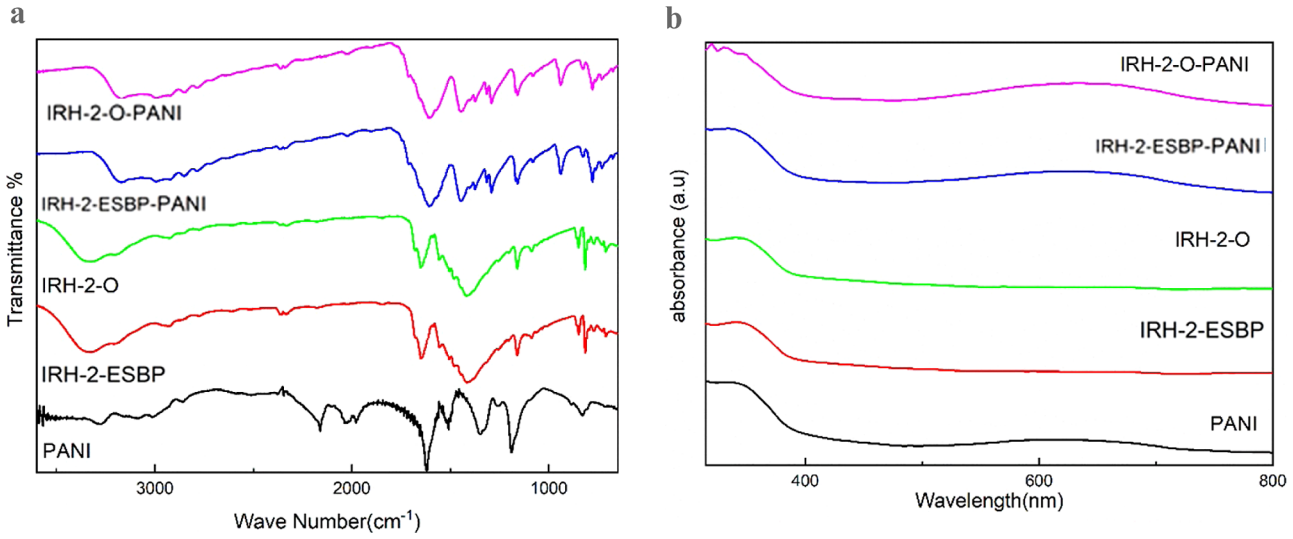

Figure 5. FTIR (a) and UV−vis (b) spectra of PANI, IRH-2-ESBP, IRH-2-O, IRH-2-ESBP/PANI, and IRH-2-O/PANI.

The final morphology of MOF crystals is influenced by various parameters related to the synthesis process such as the compatibility and geometry of precursor blocks (ligands and metal ions), as well as the kinetics and thermodynamics controlling the coordination bond formation.[62] These factors are closely related to several parameters, such as the pH, the temperature, the composition, and the polarity of the reaction solvent, and act directly on the solubility and the ionic activity of the organic ligand and of the metal ions in the reaction medium. The crystal morphology variation of IRH-2 from octahedral crystals to elongated square-bipyramidal ones can be related to the synthesis conditions change, especially the impact of the solvent composition on the ionic activity of organic linkers and metallic ions. Adding more amount of water increased the solvent polarity and the solubility of potassium cyamelurate, which led to the Kirkendall effect,[63] for which the diffusion rates of the ions increased within the growing structure layers during the crystallization process and changed the growth rates of different crystallographic facets. These results show the dependence of the crystal morphology on the reaction conditions.

SEM and EDX mapping give a view of crystal forms *versus* chemical composition. Figures S1 and S2 show that both forms have different crystal shapes, therefore they exhibit almost the same EDX surface composition. Such a result confirms that both crystal forms have the same elementary composition. From Figures 3, 4, S1, and S2, we note that the IRH-2-ESBP crystal size is practically double that of IRH-2-O due to the growth of an extra cuboid between the two pyramidal tops for IRH-2-ESBP crystals, which highlighted the preferential crystal growth along the *c*-axis and leads to cuboid formation between the two pyramids of the octahedron and elongated the crystal size. Figures S3−S6 show synthesized PANI fibers at different magnifications and confirm the desired composite formation. For IRH-2-O//PANI and IRH-2-ESBP//PANI composites, we note that MOF crystals lose their morphology. Also, we note that cerium metal atoms are not detected in the EDX mapping. Probably, the PANI fibers cover the hole external surface of the MOFs, and the thickness is enough to prevent the signal of cerium metal in EDX. From this point, we think that the pores of the MOF tunnels are blocked, and this can affect their electrochemical performance.

FTIR. Figure 5a shows the FTIR spectra of pure PANI, IRH-2-O, and IRH-2-ESBP and of IRH-2-O//PANI and IRH-2-ESBP//PANI composites. The characteristic bands of PANI functional groups located at 1508, 1624, 1350, 1190, and 828 cm^{-1} agree with the emeraldine form. The characteristic bands at 1508 and 1624 cm^{-1} are assigned to the C−C stretching vibration of quinoid rings and benzene rings, while other bonds at 1350, 1190, and 828 cm^{-1} correspond to the C−N and C−N^+ stretching vibration modes and the C−H bending mode of the benzene ring, the C−H bending mode of the quinoid ring, and the C−H out-of-plane bending vibration of the 1,4-disubstituted aromatic rings, respectively. In the 3400−2500 cm^{-1} range of the IR spectrum of PANI, we can observe the vibrational bands of N−H groups.[57,58,64] FTIR spectra of IRH-2-O and IRH-2-ESBP are identical to the published ones with no differences, which confirms the obtention of the desired IRH-2 structure.[52] In the IR spectra of IRH-2-O//PANI and IRH-2-ESBP//PANI composites, we can see the fingerprints of IRH-2 MOF and PANI; also a new band appeared at 935 cm^{-1} which could be assigned to the band between PANI and IRH-2. The presence of PANI in the composites is confirmed by the appearance of its characteristic band, especially the band at 828 cm^{-1} appeared at 830 cm^{-1} and also the band at 2030 cm^{-1} appeared at 2020 cm^{-1} in the composite's IR spectra. In general, we note a shift of all bands in the PANI fingerprint and IRH-2's fingerprints. The shift of these bands could be explained by the formation of hydrogen bonds between coordinated water molecules of IRH-2 and the polymeric chains of PANI, as suggested by Shao *et al.*[64] In fact, these interactions could result in the confinement of PANI chains in the IRH-2's pores during the *in situ* polymerization process, which restricts the vibration modes of the characteristic bands of PANI functional groups, pushing these vibration frequencies to a relatively less wavenumber.

UV−Vis Spectroscopy. The UV−vis absorption spectra shown in Figure 5b of PANI, IRH-2-O, IRH-2-ESBP, and the two composites were performed in NMP. As expected, IRH-2-O and IRH-2-ESBP did not show any absorption band in the visible region. The characteristic bands of pure PANI are observed at 340 and 632 nm, which could be attributed to the $\pi-\pi^*$ and polaron−π^* transitions in quinoid and benzoid units of polyaniline, respectively. These values are in good

https://doi.org/10.1021/acsomega.3c05385
ACS Omega 2023, 8, 43708−43718

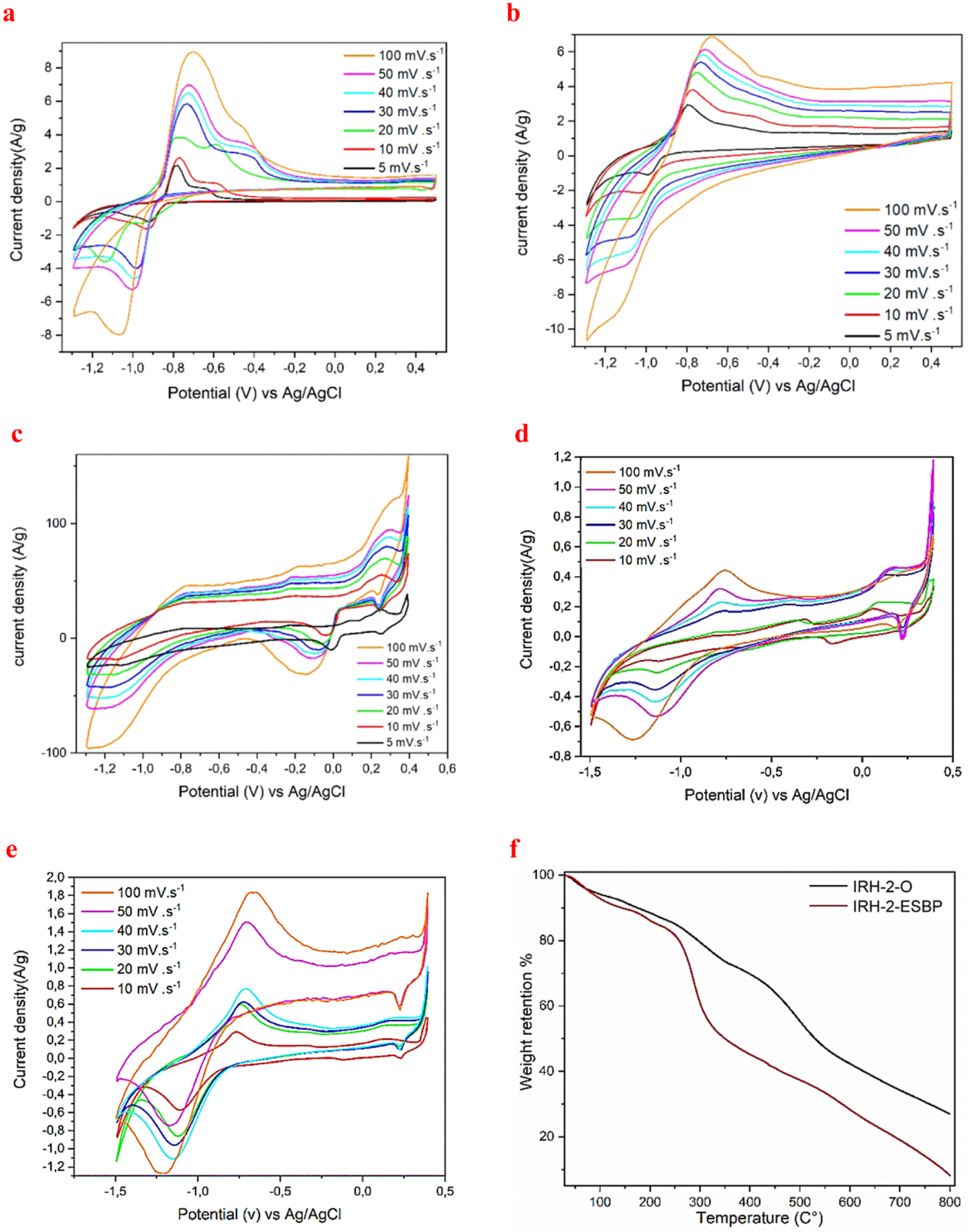

Figure 6. Voltammograms of (a) IRH-2-O, (b) IRH-2-ESBP, (c) PANI, (d) IRH-2-O/PANI, and (e) IRH-ESBP/PANI. (f) TGA curves of IRH-2-O and IRH-2-ESBP.

agreement with the literature.[65−67] The characteristic bands of PANI are also observed in the spectra of IRH-2//PANI composites, which confirm the formation of IRH-2-O//PANI and IRH-2-ESBP//PANI composites. Moreover, we observed blue shifts of the absorption bands in the composite spectra, and such shifts can be assigned to the intermolecular interactions of the PANI within the functional group of IRH-2 MOFs. FTIR and UV−vis results confirmed the probability of getting the desired composites.[64,68,69]

Electrochemical Performance. To estimate the electrochemical behavior of the prepared electrode materials, cyclic voltammograms were collected at various scan rates ranging from 5 mV·s^{-1} up to 100 mV·s^{-1} with a cell voltage equal to 1.8 V for IRH-2-O and IRH-2-ESBP, 1.8 V for the PANI

https://doi.org/10.1021/acsomega.3c05385
ACS Omega 2023, 8, 43708−43718

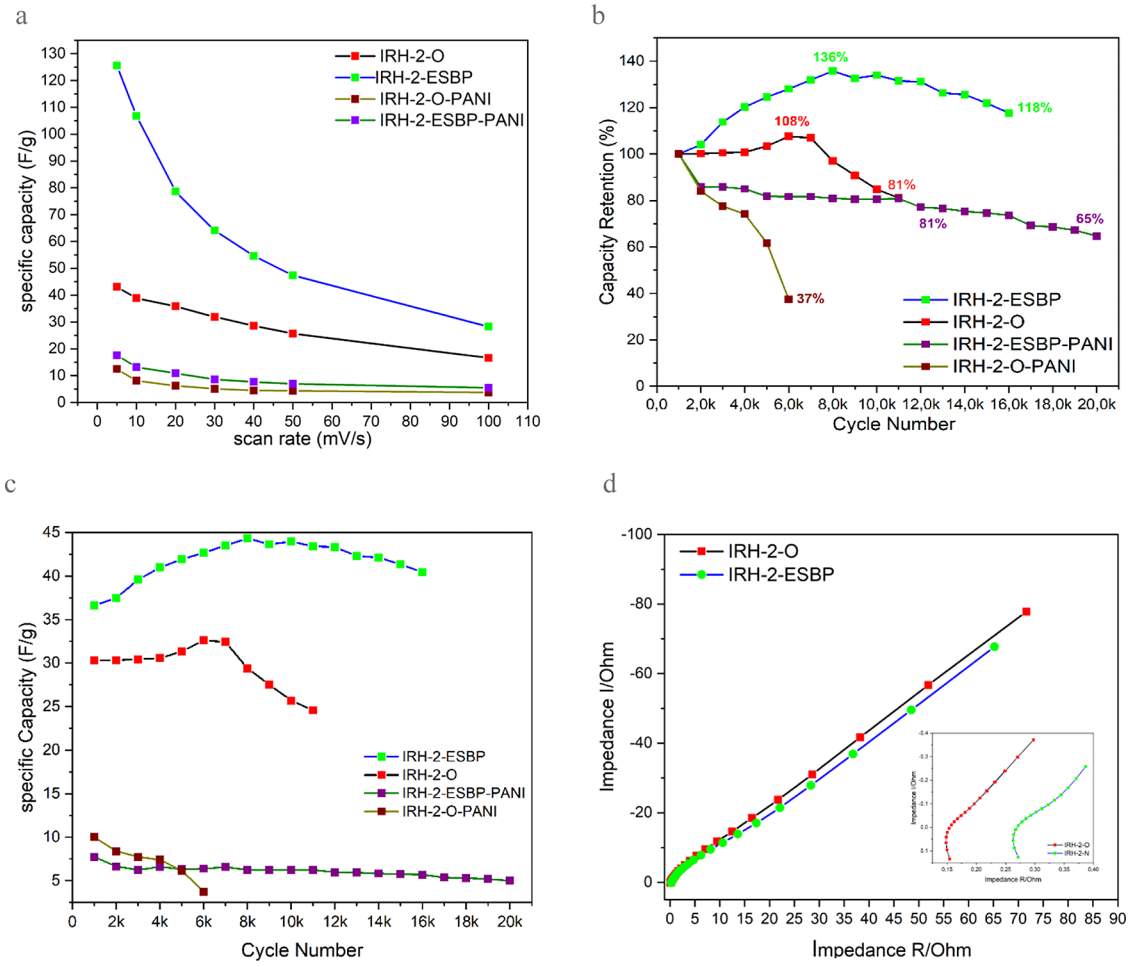

Figure 7. (a) Specific capacity, (b) capacity retention, and (c) cyclability of IRH-2-O, IRH-2-ESBP, IRH-2-O/PANI, and IRH-EO/PANI. (d) EIS of IRH-2-O and IRH-2-ESBP.

sample, and 1.95 V for IRH-2-O//PANI and IRH-2-ESBP//PANI (Figure 6). All compounds except PANI were tested from 6000 to 20 000 separated cycles until the specific capacitance decreased. As shown in Figure 6a,b, we notice that both MOFs have pseudocapacitive behavior with a quasi-reversible voltammogram shape of two high oxidation peaks at *ca.* −0.7 and −0.45 V *vs* Ag/AgCl and two reduction peaks at *ca.* −0.86 V *vs* and −1.1 V *vs* Ag/AgCl. This pseudocapacitive behavior can be related to the oxidoreduction exchanges of electrolyte anions and the open metal sites formed within the porous frameworks.[70−72]

The reticular series of IRH materials previously were characterized as microporous MOFs by Mohan *et al.*[52] In this study, the specific surface area of the cerium-based IRH-2 reached 594.5 $m^2 \cdot g^{-1}$, indicating a significant accessible surface area available for various interactions; the effective pore size aperture was calculated to be around 4.19 Å, and the total pore volume was about 0.14 $cm^3 \cdot g^{-1}$ which emphasize the presence of narrow channels within the material. These microporous features of IRH-2 offer several advantages; first, it enables the efficient insertion of electrolyte ions into the framework, facilitating their interaction with the internal surfaces. Second, it allows close contact of these ions with the exposed open metal sites within the material. This combination of features particularly enhance the electrochemical interactions between the framework and the electrolyte. As suggested by Ramachandran *et al.*,[51] cerium ions can react with OH^- anions, which can reach the accessible pores following eqs 1 and 2. Nevertheless, we notice a quadratic shape of the voltammograms of the IRH-2 MOFs and their PANI composites in the range of −0.4 to 0.5 V, which indicates a capacitive behavior due to the insertion of the electrolyte ions through the tunnels of IRH-2 and the formation of a Helmholtz double layer with the walls of the MOF tunnels.[73,74] The nitrogen-rich surface of framework walls reinforced their electrostatic interactions with electrolyte ions, which form an electric double-layer exchange phenomenon.[75,76] Compared to IRH-2-O and IRH-2-O//PANI, this phenomenon is more apparent in IRH-2-ESBP and IRH-2-ESBP//PANI voltammograms. The anisotropic crystal growth of IRH-2-ESBP leads to a higher contact of external crystal facets compared to the isotropic crystal growth of IRH-2-O that leads to a lower contact of external crystal facets, which enhances the density of open metal sites and exposed nitrogen sites in curvature and crystal facets, as well as surface charge and energy, and foster the electrochemical interactions with the electrolyte Ions. From the voltammograms shown in Figure 6d,e, we conclude that IRH-2-O//PANI and IRH-2-ESBP//PANI electrodes show practically the same electrochemical behavior of pure IRH-2-O and IRH-2-ESBP, respectively, except for the presence of the PANI oxidation peak in the case of IRH-2-O curves.

https://doi.org/10.1021/acsomega.3c05385
ACS Omega 2023, 8, 43708−43718

$$Ce(II)_s + OH^- \leftrightarrow Ce(II)_s(OH)_{ad} + e^- \quad (2)$$

$$Ce(II)_s(OH)_{ad} \leftrightarrow Ce(III)_s(OH)_{ad} + e^- \quad (3)$$

The five samples were tested at different scan rates from 5 to 100 mV·s^{-1} to study the electrochemical kinetics at high scan rates, in addition to the feasibility of electrolyte ions' insertion at different scan rates. From Figure 7a, we conclude that as the slew rate decreases the electrolyte ions have a greater chance of diffusing into the structure of the electrode material, resulting in more ion storage on the outer surface of the electrode material. Thus, at a low scan rate, in addition to the external pores, the internal pores are also involved, and the specific surface area increases; thus, the charge storage and specific capacity are improved.

All maximum specific capacitances were calculated from CV curves to be 125.57 F·g^{-1} for IRH-2-ESBP *versus* 43.1 F·g^{-1} for IRH-2-O at 5 mV·s^{-1}. This behavior can be explained by the difference in morphology between IRH-2-O and IRH-2-ESBP crystals which is characterized by the multiplicity of metallic cerium nodes and the density of nitrogen active sites on the exposed facets of crystals in the case of IRH-2-ESBP. Both forms of IRH-2 drastically lose their high capacitance when combined with PANI because of their framework's instability in the acidic media of PANI composites synthesis and because of the narrow pore apertures (Figures S5 and S6a). Despite the low PANI quantity that we used for 60:1 (MOF/PANI), the pores are probably blocked and prevent the electrolyte ions from logging into the framework. Instead of that, the electroactive domain becomes larger compared with pure PANI and pure MOFs, and the capacitance was also maintained when recycled at 50 mV·s^{-1}. In the case of IRH-2-ESBP, we note that the capacitance increases progressively after the first 1000 cycles until reaching the maximum capacity retention of 136% (Figure 7b,c). As explicated by Sankar *et al.*,[77] when the cycling process starts, the electrode does not entirely contribute to the process because the electrolyte ions do not reach the kernel of the MOF crystals. After a few cycles, the electrolyte ions penetrate the structure, and the metal-coordinated water molecules in the frameworks (Figure 1) are released continuously causing its collapse which justifies the specific capacitance decrease after 8k cycles. Sankar *et al.* also suggested another possibility, expecting solvent exchange to not occur entirely and some residual solvent remaining in the pores, as shown in TGA curves (Figure 6f), and starting to leave out after certain electrochemical exchanges. IRH-2-O reacted to the cyclization in the same way, but it is noted that after reaching the maximum of 108%, its capacity retention was drastically decreased, which reflects the structure frailness of IRH-2-O compared to IRH-2-ESBP which maintained 118% of its specific capacity after 16k cycles. The IRH-2-ESBP/PANI composite responded differently from the IRH-2-ESBP; after the drop in the specific capacity retention percentage compared with the first 1000 cycles, the value remains stable at around 80% until 16k cycles and then starts to decrease to reach 65% at 20k. After the cyclization process, PXRD analyses were carried out, as illustrated in Figure S7. These PXRD patterns provide valuable insights into the structural characteristics of the materials after cyclization. The PXRD patterns clearly demonstrate that the characteristic peaks of IRH-2 are still present after cyclization. This retention of IRH-2's characteristic peaks indicates that the IRH-2 MOFs maintain their structural stability even after undergoing cyclization. This stability is a noteworthy finding, as it suggests that the essential structural features of IRH-2 are preserved throughout the process. It is also worth noting that the patterns of IRH-2-O and IRH-2-ESBP were likely analyzed to compare any differences or modifications in their PXRD profiles after the cyclization process. These findings are valuable in assessing how various treatments or modifications may impact the structural integrity of the MOFs. Overall, the PXRD analyses provide crucial evidence of the stability of IRH-2 MOFs following cyclization and offer insights into their structural characteristics.

To evaluate the charge-transfer phenomenon based on the concept of frequency in a detailed manner, an electrochemical impedance spectroscopy (EIS) investigation was performed at the frequency of 100 kHz to 1 MHz. Figure 7d illustrates two EIS curves of IRH-2-O and IRH-2-ESBP with typical look of a pseudocapacitive material.[51,78] As expected, the faradic behavior of IRH-2-O and IRH-2-ESBP was depicted by the presence of a semiarc at low frequencies. The imaginary part of the plot increases vertically in the high frequency range, which highlights the good capacitive performance of both the electrodes and further shows the improvement noted after the use of the porous frameworks in the presence of PANI.

Surface chemical compositions and valence states of IRH-2-O and IRH-2-ESBP were extensively probed using X-ray photoelectron spectroscopy (XPS). Survey spectra in Figure S9 unequivocally confirm the presence of carbon, oxygen, nitrogen, and cerium, integral components of these materials' composition. Notably, the Ce 3d XPS spectra in Figure S9b unambiguously reveal the coexistence of Ce^{3+} and Ce^{4+} within the samples, as manifested by characteristic peaks at approximately 885 and 900 eV for Ce^{3+} and at 882, 898, 903, and 916 eV for Ce^{4+}.[79] These findings strongly reinforce our proposition that the surface of the material is the site of the reaction, underscoring the pivotal role played by different cerium valence states. This insight significantly advances our comprehension of the materials surface chemistry and our desired application.

CONCLUSIONS

In summary, we successfully synthesized two different crystal forms of cerium-based MOFs denoted IRH-2-O and IRH-2-ESBP comprising octahedral and elongated square-bipyramidal crystals, respectively. SCXRD and PXRD analyses showed an identical crystal structure and composition for both MOFs. The anisotropic crystal growth of these materials was highlighted by SEM and EDX mapping analyses, the difference in their synthesis conditions leading to an isotropic growth of a homogeneous phase of octahedral crystals for IRH-2-O with an average particle size of 107.3 μm and an anisotropic growth of the elongated square- bipyramidal crystals for IRH-2-ESBP with an average particle size of 198.9 μm. We demonstrated the significant effect of the tunable anisotropic crystal shapes of IRH-2 to enhance the density of open cerium sites and nitrogen-active sites on the exposed crystal facets and improve the electrochemical performances of IRH-2 as a supercapacitor electrode. The specific capacitance of IRH-2-ESBP reaches 125.57 F·g^{-1} compared to 43.1 F·g^{-1} for IRH-2-O at 5 mV·s^{-1}. IRH-2-ESBP shows very high stability reaching 20 000 cycles compared to IRH-2-O with 8k cycles. The composite with PANI contributed to increasing the cell voltage up to 1.95, but a decrease in the electrochemical performance was observed for all IRH-2/PANI composites and has been explained by the

https://doi.org/10.1021/acsomega.3c05385
ACS Omega 2023, 8, 43708−43718

instability of IRH-2 in the acidic conditions of composite synthesis.

■ ASSOCIATED CONTENT

Supporting Information

The Supporting Information is available free of charge at https://pubs.acs.org/doi/10.1021/acsomega.3c05385.

SEM images and EDX mapping for all synthesized materials, PXRD spectra after CV cyclization, and XPS analysis spectra (PDF)

■ AUTHOR INFORMATION

Corresponding Authors

Najmeddine Ferhi − *Département de Chimie, Biochimie et physique and Institut de Recherche sur l'Hydrogène, Université du Québec à Trois-Rivières, Trois-Rivières, Québec G9A 5H7, Canada*; Email: Najmeddine.Ferhi@uqtr.ca

Ramzi Zarrougui − *Département des sciences fondamentales, Université du Québec à Chicoutimi, Chicoutimi, Québec G7H 2B1, Canada*; orcid.org/0000-0003-4930-2037; Email: ramzi_zarrougui@uqac.ca

Author

Mohamed Essalhi − *Département de Chimie, Biochimie et physique and Institut de Recherche sur l'Hydrogène, Université du Québec à Trois-Rivières, Trois-Rivières, Québec G9A 5H7, Canada*

Complete contact information is available at: https://pubs.acs.org/10.1021/acsomega.3c05385

Notes

The authors declare no competing financial interest.

■ ACKNOWLEDGMENTS

We are grateful to the support of Natural Sciences and Engineering Research Council of Canada (RGPIN-2015-06425), the Fonds de recherche du Québec—Nature et Technologies, and The Canadian Foundation for Innovation and Université du Québec à Trois-Rivières. We also thank Professor Pierre Bénard, Raphael Gervais Lavoie, and Dr Moomen Marzouki for their support and valuable advice.

■ REFERENCES

(1) Chapman, A. J.; Itaoka, K. Energy Transition to a Future Low-Carbon Energy Society in Japan's Liberalizing Electricity Market: Precedents, Policies and Factors of Successful Transition. *Renewable Sustainable Energy Rev.* **2018**, *81*, 2019−2027.

(2) Zhou, L.; Li, J.; Li, F.; Meng, Q.; Li, J.; Xu, X. Energy Consumption Model and Energy Efficiency of Machine Tools: A Comprehensive Literature Review. *J. Cleaner Prod.* **2016**, *112*, 3721−3734.

(3) Hu, H.; Xue, W.; Jiang, P.; Li, Y. Bibliometric Analysis for Ocean Renewable Energy: An Comprehensive Review for Hotspots, Frontiers, and Emerging Trends. *Renewable Sustainable Energy Rev.* **2022**, *167*, 112739.

(4) Paramati, S. R.; Shahzad, U.; Doğan, B. The Role of Environmental Technology for Energy Demand and Energy Efficiency: Evidence from OECD Countries. *Renewable Sustainable Energy Rev.* **2022**, *153*, 111735.

(5) Sorrell, S. Reducing Energy Demand: A Review of Issues, Challenges and Approaches. *Renewable Sustainable Energy Rev.* **2015**, *47*, 74−82.

(6) Chen, C.; Pinar, M.; Stengos, T. Determinants of Renewable Energy Consumption: Importance of Democratic Institutions. *Renewable Energy* **2021**, *179*, 75−83.

(7) Abas, N.; Kalair, A.; Khan, N. Review of Fossil Fuels and Future Energy Technologies. *Futures* **2015**, *69*, 31−49.

(8) Papież, M.; Śmiech, S.; Frodyma, K.; Borowiec, J. Decoupling Is Not Enough - Evidence from Fossil Fuel Use in over 130 Countries. *J. Cleaner Prod.* **2022**, *379*, 134856.

(9) Ahmed, K.; Ozturk, I. What New Technology Means for the Energy Demand in China? A Sustainable Development Perspective. *Environ. Sci. Pollut. Res.* **2018**, *25* (29), 29766−29771.

(10) Pimentel, D.; Whitecraft, M.; Scott, Z. R.; Zhao, L.; Satkiewicz, P.; Scott, T. J.; Phillips, J.; Szimak, D.; Singh, G.; Gonzalez, D. O.; Moe, T. L. Will Limited Land, Water, and Energy Control Human Population Numbers in the Future? *Hum. Ecol.* **2010**, *38* (5), 599−611.

(11) Rehman, A.; Rauf, A.; Ahmad, M.; Chandio, A. A.; Deyuan, Z. The Effect of Carbon Dioxide Emission and the Consumption of Electrical Energy, Fossil Fuel Energy, and Renewable Energy, on Economic Performance: Evidence from Pakistan. *Environ. Sci. Pollut. Res.* **2019**, *26* (21), 21760−21773.

(12) Li, B.; Haneklaus, N. The Role of Renewable Energy, Fossil Fuel Consumption, Urbanization and Economic Growth on CO2 Emissions in China. *Energy Rep.* **2021**, *7*, 783−791.

(13) Abbasi, K. R.; Shahbaz, M.; Zhang, J.; Irfan, M.; Alvarado, R. Analyze the Environmental Sustainability Factors of China: The Role of Fossil Fuel Energy and Renewable Energy. *Renewable Energy* **2022**, *187*, 390−402.

(14) Overland, I.; Juraev, J.; Vakulchuk, R. Are Renewable Energy Sources More Evenly Distributed than Fossil Fuels? *Renewable Energy* **2022**, *200*, 379−386.

(15) Wang, D.; Han, C.; Mo, F.; Yang, Q.; Zhao, Y.; Li, Q.; Liang, G.; Dong, B.; Zhi, C. Energy Density Issues of Flexible Energy Storage Devices. *Energy Storage Mater.* **2020**, *28*, 264−292.

(16) Lv, Z.; Li, W.; Yang, L.; Loh, X. J.; Chen, X. Custom-Made Electrochemical Energy Storage Devices. *ACS Energy Lett.* **2019**, *4* (2), 606−614.

(17) Kong, L.; Liu, M.; Huang, H.; Xu, Y.; Bu, X. H. Metal/Covalent-Organic Framework Based Cathodes for Metal-Ion Batteries. *Adv. Energy Mater.* **2022**, *12* (4), 2100172.

(18) Liu, Z.; Huang, Y.; Huang, Y.; Yang, Q.; Li, X.; Huang, Z.; Zhi, C. Voltage Issue of Aqueous Rechargeable Metal-Ion Batteries. *Chem. Soc. Rev.* **2020**, *49* (1), 180−232.

(19) Olabi, A. G.; Sayed, E. T.; Wilberforce, T.; Jamal, A.; Alami, A. H.; Elsaid, K.; Rahman, S. M. A.; Shah, S. K.; Abdelkareem, M. A. Metal-Air Batteries—A Review. *Energies* **2021**, *14* (21), 7373.

(20) Lai, C. S.; Locatelli, G. Economic and Financial Appraisal of Novel Large-Scale Energy Storage Technologies. *Energy* **2021**, *214*, 118954.

(21) Shan, R.; Reagan, J.; Castellanos, S.; Kurtz, S.; Kittner, N. Evaluating Emerging Long-Duration Energy Storage Technologies. *Renewable Sustainable Energy Rev.* **2022**, *159*, 112240.

(22) Wu, Y.; Zhang, T.; Gao, R.; Wu, C. Portfolio Planning of Renewable Energy with Energy Storage Technologies for Different Applications from Electricity Grid. *Appl. Energy* **2021**, *287*, 116562.

(23) Iqbal, M. Z.; Aziz, U. Supercapattery: Merging of Battery-Supercapacitor Electrodes for Hybrid Energy Storage Devices. *J. Energy Storage* **2022**, *46*, 103823.

(24) Das, A.; Raj, B.; Mohapatra, M.; Andersen, S. M.; Basu, S. Performance and Future Directions of Transition Metal Sulfide-Based Electrode Materials towards Supercapacitor/Supercapattery. *Wiley Interdiscip. Rev.: Energy Environ.* **2022**, *11* (1), No. e414.

(25) Schmidt, O.; Hawkes, A.; Gambhir, A.; Staffell, I. The Future Cost of Electrical Energy Storage Based on Experience Rates. *Nat. Energy* **2017**, *2* (8), 17110.

(26) Nadeem, F.; Hussain, S. M. S.; Tiwari, P. K.; Goswami, A. K.; Ustun, T. S. Comparative Review of Energy Storage Systems, Their Roles, and Impacts on Future Power Systems. *IEEE Access* **2019**, *7*, 4555−4585.

(27) Hadjipaschalis, I.; Poullikkas, A.; Efthimiou, V. Overview of Current and Future Energy Storage Technologies for Electric Power Applications. *Renewable Sustainable Energy Rev.* **2009**, *13* (6−7), 1513−1522.
(28) Navarro, G.; Torres, J.; Blanco, M.; Nájera, J.; Santos-Herran, M.; Lafoz, M. Present and Future of Supercapacitor Technology Applied to Powertrains, Renewable Generation and Grid Connection Applications. *Energies* **2021**, *14* (11), 3060.
(29) Rajak, R.; Kumar, R.; Ansari, S. N.; Saraf, M.; Mobin, S. M. Recent Highlights and Future Prospects on Mixed-Metal MOFs as Emerging Supercapacitor Candidates. *Dalton Trans.* **2020**, *49* (34), 11792−11818.
(30) Gidwani, M.; Bhagwani, A.; Rohra, N. Supercapacitors: The near Future of Batteries. *Int. J. Eng. Invent.* **2014**, *4* (5), 22−27.
(31) Karthikeyan, S.; Narenthiran, B.; Sivanantham, A.; Bhatlu, L. D.; Maridurai, T. Supercapacitor: Evolution and Review. *Mater. Today: Proc.* **2021**, *46*, 3984−3988.
(32) Wang, Y.; Zhang, L.; Hou, H.; Xu, W.; Duan, G.; He, S.; Liu, K.; Jiang, S. Recent Progress in Carbon-Based Materials for Supercapacitor Electrodes: A Review. *J. Mater. Sci.* **2021**, *56* (1), 173−200.
(33) Poonam; Sharma, K.; Arora, A.; Tripathi, S. K. Review of Supercapacitors: Materials and Devices. *J. Energy Storage* **2019**, *21*, 801−825.
(34) Young, C.; Kim, J.; Kaneti, Y. V.; Yamauchi, Y. One-Step Synthetic Strategy of Hybrid Materials from Bimetallic Metal-Organic Frameworks for Supercapacitor Applications. *ACS Appl. Energy Mater.* **2018**, *1* (5), 2007−2015.
(35) Peng, H.; Raya, J.; Richard, F.; Baaziz, W.; Ersen, O.; Ciesielski, A.; Samorì, P. Synthesis of Robust MOFs@COFs Porous Hybrid Materials via an Aza-Diels-Alder Reaction: Towards High-Performance Supercapacitor Materials. *Angew. Chem., Int. Ed.* **2020**, *59* (44), 19602−19609.
(36) Ayman, I.; Rasheed, A.; Ajmal, S.; Rehman, A.; Ali, A.; Shakir, I.; Warsi, M. F. CoFe2O4Nanoparticle-Decorated 2D MXene: A Novel Hybrid Material for Supercapacitor Applications. *Energy Fuels* **2020**, *34* (6), 7622−7630.
(37) Zhang, X.; Hou, L.; Ciesielski, A.; Samorì, P. 2D Materials Beyond Graphene for High-Performance Energy Storage Applications. *Adv. Energy Mater.* **2016**, *6* (23), 1600671.
(38) Zhai, S.; Wei, L.; Karahan, H. E.; Chen, X.; Wang, C.; Zhang, X.; Chen, J.; Wang, X.; Chen, Y. 2D Materials for 1D Electrochemical Energy Storage Devices. *Energy Storage Mater.* **2019**, *19*, 102−123.
(39) Cui, H.; Guo, Y.; Ma, W.; Zhou, Z. 2 D Materials for Electrochemical Energy Storage: Design, Preparation, and Application. *ChemSusChem* **2020**, *13* (6), 1155−1171.
(40) Kumar, R.; Sahoo, S.; Joanni, E.; Singh, R. K.; Kar, K. K. Microwave as a Tool for Synthesis of Carbon-Based Electrodes for Energy Storage. *ACS Appl. Mater. Interfaces* **2022**, *14*, 20306−20325.
(41) Dong, Y.; Wu, Z. S.; Ren, W.; Cheng, H. M.; Bao, X. Graphene: A Promising 2D Material for Electrochemical Energy Storage. *Sci. Bull.* **2017**, *62* (10), 724−740.
(42) Wu, L.; Li, Y.; Fu, Z.; Su, B. L. Hierarchically Structured Porous Materials: Synthesis Strategies and Applications in Energy Storage. *Natl. Sci. Rev.* **2020**, *7* (11), 1667−1701.
(43) Bennett, T. D.; Coudert, F. X.; James, S. L.; Cooper, A. I. The Changing State of Porous Materials. *Nat. Mater.* **2021**, *20* (9), 1179−1187.
(44) Du, R.; Wu, Y.; Yang, Y.; Zhai, T.; Zhou, T.; Shang, Q.; Zhu, L.; Shang, C.; Guo, Z. Porosity Engineering of MOF-Based Materials for Electrochemical Energy Storage. *Adv. Energy Mater.* **2021**, *11* (20), 2100154.
(45) Radhakrishnan, S.; Selvaraj, S. C.; Kim, B. S. Morphology Engineering of Co-MOF Nanostructures to Tune Their Electrochemical Performances for Electrocatalyst and Energy-Storage Applications Supported by DFT Studies. *Appl. Surf. Sci.* **2022**, *605*, 154691.
(46) Peng, Y.; Xu, J.; Xu, J.; Ma, J.; Bai, Y.; Cao, S.; Zhang, S.; Pang, H. Metal-Organic Framework (MOF) Composites as Promising Materials for Energy Storage Applications. *Adv. Colloid Interface Sci.* **2022**, *307*, 102732.
(47) Zhan, F.; Liu, S.; He, Q.; Zhao, X.; Wang, H.; Han, M.; Yamauchi, Y.; Chen, L. Metal-Organic Framework-Derived Heteroatom-Doped Nanoarchitectures for Electrochemical Energy Storage: Recent Advances and Future Perspectives. *Energy Storage Mater.* **2022**, *52*, 685−735.
(48) Xu, J.; Peng, Y.; Xing, W.; Ding, Z.; Zhang, S.; Pang, H. Metal-Organic Frameworks Marry Carbon: Booster for Electrochemical Energy Storage. *J. Energy Storage* **2022**, *53*, 105104.
(49) Lokhande, P. E.; Kulkarni, S.; Chakrabarti, S.; Pathan, H. M.; Sindhu, M.; Kumar, D.; Singh, J.; Kumar, A.; Kumar Mishra, Y.; Toncu, D. C.; Syväjärvi, M.; Sharma, A.; Tiwari, A. The Progress and Roadmap of Metal-Organic Frameworks for High-Performance Supercapacitors. *Coord. Chem. Rev.* **2022**, *473*, 214771.
(50) Khan, U. A.; Iqbal, N.; Noor, T.; Ahmad, R.; Ahmad, A.; Gao, J.; Amjad, Z.; Wahab, A. Cerium Based Metal Organic Framework Derived Composite with Reduced Graphene Oxide as Efficient Supercapacitor Electrode. *J. Energy Storage* **2021**, *41*, 102999.
(51) Ramachandran, R.; Xuan, W.; Zhao, C.; Leng, X.; Sun, D.; Luo, D.; Wang, F. Enhanced Electrochemical Properties of Cerium Metal-Organic Framework Based Composite Electrodes for High-Performance Supercapacitor Application. *RSC Adv.* **2018**, *8* (7), 3462−3469.
(52) Mohan, M.; Essalhi, M.; Durette, D.; Rana, L. K.; Ayevide, F. K.; Maris, T.; Duong, A. A Rational Design of Microporous Nitrogen-Rich Lanthanide Metal-Organic Frameworks for CO2/CH4Separation. *ACS Appl. Mater. Interfaces* **2020**, *12* (45), 50619−50627.
(53) Xu, G.; Nie, P.; Dou, H.; Ding, B.; Li, L.; Zhang, X. Exploring Metal Organic Frameworks for Energy Storage in Batteries and Supercapacitors. *Mater. Today* **2017**, *20* (4), 191−209.
(54) Suresh, K.; Kalenak, A. P.; Sotuyo, A.; Matzger, A. J. Metal-Organic Framework (MOF) Morphology Control by Design. *Chem.—Eur. J.* **2022**, *28* (18), No. e202200334.
(55) Gittins, J. W.; Balhatchet, C. J.; Fairclough, S. M.; Forse, A. C. Enhancing the Energy Storage Performances of Metal-Organic Frameworks by Controlling Microstructure. *Chem. Sci.* **2022**, *13* (32), 9210−9219.
(56) Holst, J. R. Synthesis of Inorganic Heptazine-Based Materials. Ph.D. Thesis, University of Iowa, 2009.
(57) Zhao, Y.; Arowo, M.; Wu, W.; Chen, J. Effect of Additives on the Properties of Polyaniline Nanofibers Prepared by High Gravity Chemical Oxidative Polymerization. *Langmuir* **2015**, *31* (18), 5155−5163.
(58) Liao, Y.; Zhang, C.; Zhang, Y.; Strong, V.; Tang, J.; Li, X. G.; Kalantar-Zadeh, K.; Hoek, E. M. V.; Wang, K. L.; Kaner, R. B. Carbon Nanotube/Polyaniline Composite Nanofibers: Facile Synthesis and Chemosensors. *Nano Lett.* **2011**, *11* (3), 954−959.
(59) Ferhi, N.; Desalegn Assresahegn, B.; Ardila-Suarez, C.; Dissem, N.; Guay, D.; Duong, A. Defective Metal-Organic Framework-808@ Polyaniline Composite Materials for High Capacitance Retention Supercapacitor Electrodes. *ACS Appl. Energy Mater.* **2022**, *5* (1), 1235−1243.
(60) Lee, G.; Lee, S.; Oh, S.; Kim, D.; Oh, M. Tip-To-Middle Anisotropic MOF-On-MOF Growth with a Structural Adjustment. *J. Am. Chem. Soc.* **2020**, *142* (6), 3042−3049.
(61) Choi, S.; Kim, T.; Ji, H.; Lee, H. J.; Oh, M. Isotropic and Anisotropic Growth of Metal-Organic Framework (MOF) on MOF: Logical Inference on MOF Structure Based on Growth Behavior and Morphological Feature. *J. Am. Chem. Soc.* **2016**, *138* (43), 14434−14440.
(62) Suresh, K.; Kalenak, A. P.; Sotuyo, A.; Matzger, A. J. Metal-Organic Framework (MOF) Morphology Control by Design. *Chem.—Eur. J.* **2022**, *28*, No. e202200334.
(63) Sun, J.; Yu, X.; Zhao, S.; Chen, H.; Tao, K.; Han, L. Solvent-Controlled Morphology of Amino-Functionalized Bimetal Metal-Organic Frameworks for Asymmetric Supercapacitors. *Inorg. Chem.* **2020**, *59* (16), 11385−11395.
(64) Shao, L.; Wang, Q.; Ma, Z.; Ji, Z.; Wang, X.; Song, D.; Liu, Y.; Wang, N. A High-Capacitance Flexible Solid-State Supercapacitor

https://doi.org/10.1021/acsomega.3c05385
ACS Omega 2023, 8, 43708−43718

Based on Polyaniline and Metal-Organic Framework (UiO-66) Composites. *J. Power Sources* **2018**, *379*, 350−361.
(65) Majumdar, S.; Baishya, A.; Mahanta, D. Kinetic and Equilibrium Modeling of Anionic Dye Adsorption on Polyaniline Emeraldine Salt: Batch and Fixed Bed Column Studies. *Fibers Polym.* **2019**, *20* (6), 1226−1235.
(66) Mamma, K.; Siraj, K.; Meka, N. Synthesis and Effect of Secondary Dopant on the Conductivity of Conducting Polymer Polyaniline. *J. Polym. Eng.* **2013**, *33* (9), 785−792.
(67) Huang, W. S.; MacDiarmid, A. G. Optical Properties of Polyaniline. *Polymer* **1993**, *34* (9), 1833−1845.
(68) Li, Z.; Li, Y.; Lin, W.; Zheng, F.; Laven, J. Polyaniline/Silver Nanocomposites Synthesized via UV-Vis-Assisted Aniline Polymerization with a Reversed Micellar Microemulsion System. *Polym. Compos.* **2016**, *37* (4), 1064−1071.
(69) Mashao, G.; Modibane, K. D.; Mdluli, S. B.; Iwuoha, E. I.; Hato, M. J.; Makgopa, K.; Molapo, K. M. Polyaniline-Cobalt Benzimidazolate Zeolitic Metal-Organic Framework Composite Material for Electrochemical Hydrogen Gas Sensing. *Electrocatalysis* **2019**, *10* (4), 406−419.
(70) Sheberla, D.; Bachman, J. C.; Elias, J. S.; Sun, C. J.; Shao-Horn, Y.; Dincă, M. Conductive MOF Electrodes for Stable Supercapacitors with High Areal Capacitance. *Nat. Mater.* **2017**, *16* (2), 220−224.
(71) Kaipannan, S.; Marappan, S. Fabrication of 9.6 V High-Performance Asymmetric Supercapacitors Stack Based on Nickel Hexacyanoferrate-Derived Ni(OH)2 Nanosheets and Bio-Derived Activated Carbon. *Sci. Rep.* **2019**, *9* (1), 1104.
(72) Rahmanifar, M. S.; Hesari, H.; Noori, A.; Masoomi, M. Y.; Morsali, A.; Mousavi, M. F. A Dual Ni/Co-MOF-Reduced Graphene Oxide Nanocomposite as a High Performance Supercapacitor Electrode Material. *Electrochim. Acta* **2018**, *275*, 76−86.
(73) Pokharel, J.; Gurung, A.; Baniya, A.; He, W.; Chen, K.; Pathak, R.; Lamsal, B. S.; Ghimire, N.; Zhou, Y. MOF-Derived Hierarchical Carbon Network as an Extremely-High-Performance Supercapacitor Electrode. *Electrochim. Acta* **2021**, *394*, 139058.
(74) Zhu, G.; Wen, H.; Ma, M.; Wang, W.; Yang, L.; Wang, L.; Shi, X.; Cheng, X.; Sun, X.; Yao, Y. A Self-Supported Hierarchical Co-MOF as a Supercapacitor Electrode with Ultrahigh Areal Capacitance and Excellent Rate Performance. *Chem. Commun.* **2018**, *54* (74), 10499−10502.
(75) Yadav, S.; Devi, A. Recent Advancements of Metal Oxides/Nitrogen-Doped Graphene Nanocomposites for Supercapacitor Electrode Materials. *J. Energy Storage* **2020**, *30*, 101486.
(76) Ma, X. Q.; Zhang, B.; Xu, Z. X.; Tan, Y.; Li, B.; Zhang, Y. C.; Ni, G. S.; Zhou, W. Y.; Luque, R.; Zhang, H. Y. N-Rich and O-Poor Doped Carbon Prepared via Facile Ammonium Nitrate Assisted Hydrothermal Carbonization for Robust Supercapacitors. *J. Cleaner Prod.* **2022**, *373*, 133903.
(77) Sankar, S.; Ahmed, A. T. A.; Inamdar, A. I.; Im, H.; Im, Y. B.; Lee, Y.; Kim, D. Y.; Lee, S. Biomass-Derived Ultrathin Mesoporous Graphitic Carbon Nanoflakes as Stable Electrode Material for High-Performance Supercapacitors. *Mater. Des.* **2019**, *169*, 107688.
(78) Saravanakumar, B.; Ramachandran, S. P.; Ravi, G.; Ganesh, V.; Ravichandran, S.; Muthu Mareeswaran, P.; Yuvakkumar, R. Enhanced Pseudocapacitive Performance of SnO2, Zn-SnO2, and Ag-SnO2 Nanoparticles. *Ionics* **2018**, *24* (12), 4081−4092.
(79) Polyak, Y.; Bastl, Z. XPS and Factor Analysis Study of Initial Stages of Cerium Oxide Growth on Polycrystalline Tungsten. *Surf. Interface Anal.* **2015**, *47* (6), 663−671.

https://doi.org/10.1021/acsomega.3c05385
ACS Omega 2023, 8, 43708−43718